doi:10.1038/nature12186

S1. WANNIER DIAGRAM

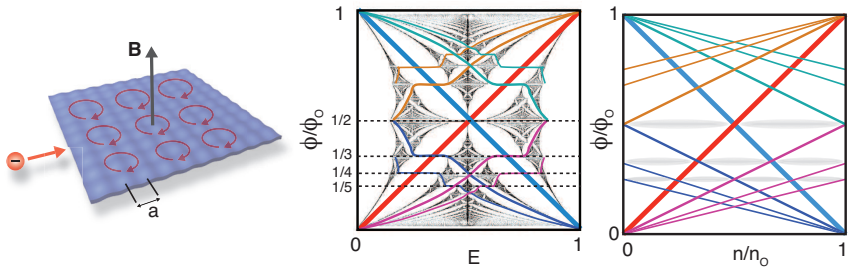

FIG. S1: Left is a cartoon image of an electron subjected to both a magnetic field, and a square periodic lattice. The usual Hofstadter Butterfly spectrum, calculated for a square superlattice, is shown in the middle. Right shows the spectrum replotted as density versus magnetic field. Coloured lines in the Hofstadter energy-field spectrum (middle) follow lines of constant chemical potential. In the Wannier density-field spectrum (right), these same lines follow linear trajectories, according to the Diophantine equation.

Fig. S1b and S1c illustrates the relationship between the energy-field diagram and density-field diagram. As first demonstrated by Wannier (see main text), all spectral gaps follow linear trajectories in the density-field space according to a dimensionless Diophantine equation (Eqn. 1 in the main text). The Wannier diagram is experimentally accessible by performing transport measurement while varying the carrier density and magnetic field. In the quantum Hall regime, spectral gaps in the spectrum appear as minima in longitudinal resistance, R_{xx}, and quantized plateaus in the transverse Hall resistance, R_{xy}.

S2. REPLOTTING LANDAU FAN DIAGRAM IN DIMENSIONLESS UNITS

The relevant quantities in the Landau fan diagram for a 2D electron system with a superimposed periodic potential are the size of the superlattice unit cell, and the number of flux penetrating this unit cell. For a square superlattice the magnetic flux penetrating the unit cell is

$$\frac{\phi}{\phi_o} = \frac{Ba^2}{\phi_o} \tag{1}$$

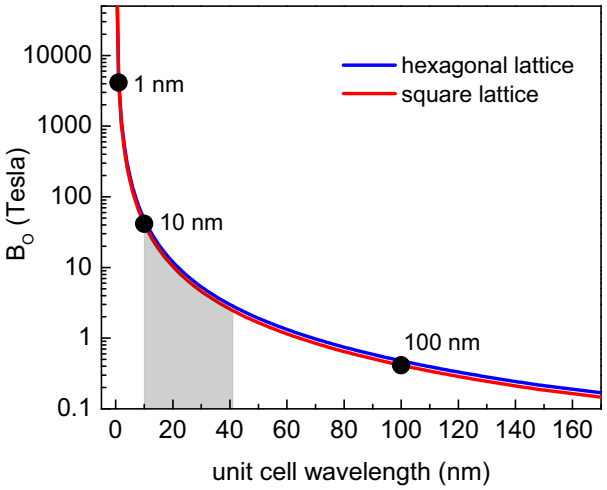

FIG. S2: Critical field versus unit cell length, defined where the ratio $\phi/\phi_o \to 1$. Gray shaded area highlights the ideal unit cell length for magnetic fields achievable in the laboratory.

where, B is the applied magnetic field, a^2 is the unit cell area, and $\phi_o = h/e$ is the magnetic flux quantum. For a hexagonal superlattice, the unit cell area is $\frac{\sqrt{3}}{2}a^2$ where a is the unit cell basis vector, giving

$$\frac{\phi}{\phi_o} = \frac{eB\sqrt{3}a^2}{2h} \tag{2}$$

We also normalize the electron density by the inverse area of the unit cell, i.e., $n \to n/n_o$, where

$$n_o = \frac{1}{unit\,cell\,area} = \frac{1}{\frac{\sqrt{3}}{2}a^2} \tag{3}$$

We can define the critical field as the field were $\phi/\phi_o \to 1$, *i.e.* when the magnetic length approaches the scale were there is approximately 1 flux quantum per unit cell area. From 1 and 2, this gives the corresponding critical magnetic field

$$B_o = \frac{2h}{\sqrt{3}ea^2} \tag{4}$$

The same analysis for a square lattice gives $B_o = h/(ea^2)$. Fig. S2 shows the critical field versus unit cell wavelength. The ideal unit cell length is highlighted in the grey shaded region, spanning the magnetic field range from a few Tesla up to approximately 40 Tesla.

S3. MOIRÉ SUPERLATTICES IN BILAYER GRAPHENE ON HBN

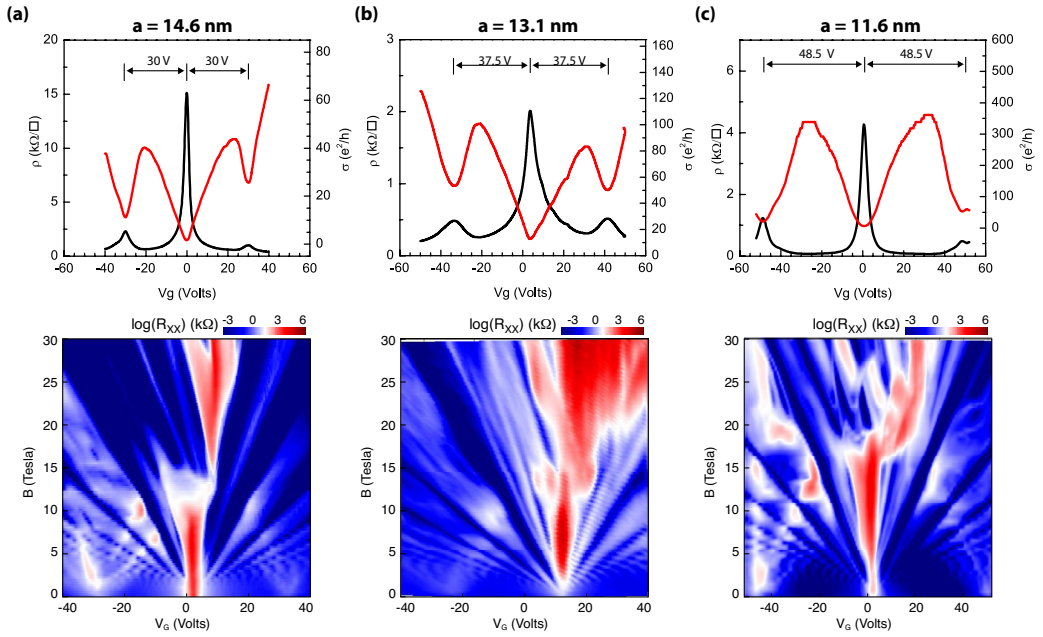

FIG. S3: (a)-(c) shows transport measured at zero magnetic field (top panel) and corresponding R_{xx} plotted in a Landau fan diagram (bottom panel), for three different devices, which we label here S1,S2 and s3. In each panel, a indicates the corresponding moiré wavelength, determined from the position of the satellite resistance peaks at zero field (see text).

Fig. S3 shows three different bilayer graphene/hBN devices that exhibit modulated transport due to the presence of a moiré pattern. Device s1 (Fig. S3a) corresponds to the device in Fig. 2 of the main text, with the longest moiré wavelength observed in our devices, s3 (Fig. S3c) corresponds to Fig. 3 of the main text, with the shortest moiré wavelength amongst our devices. Device s2 (Fig. S3b) shows a device with an intermediate moiré wavelength. Assuming a filled band model the moiré wavelength was determined from the satellite peak position according to

$$\frac{n_{sat}}{n_o} = g_s g_v \tag{5}$$

where n_{sat} is the field-effect density at the satellite peak position, $n_o = 1/A$ where $A = \sqrt{3}a^2/2$ is the unit cell area of the moiré pattern (assuming hexagonal symmetry; see Fig. 1 in the main text) with a the moiré wavelength, g_s is the electron spin degeneracy and g_v is the

valley, or pseudospin, degeneracy. n_{sat} is calculated according to a standard parallel plate capacitor model to be $n_{sat} = C_g(V_{sat} - V_{CNP})/e$, where C_g is the geometric capacitance, V_{sat} is the gate voltage corresponding to the position of the satellite resistance peak and V_{CNP} is the gate voltage corresponding the central charge neutrality peak. Substituting back into equation 5 and solving for the moiré wavelength gives

$$a = \sqrt{\frac{8e}{\sqrt{3}C_g(V_{sat} - V_{CNP})}} \tag{6}$$

For the three devices in Fig S3, the satellite peaks appear at 30 V, ,37.5 V, and 48.5 V, giving moiré wavelengths 14.6 nm, 13.1 nm and 11.6 nm, respectively.

S4. SYMMETRY BREAKING

We note that the most prominent fractal gap states within the lowest Landau level of all devices correspond to positive s, but negative t quantum numbers. Likewise, the overall fractal gap structure appears stronger on the hole side (negative density values) than the electron side (positive density values). This electron/hole asymmetry results from coupling between BLG and hBN, which, in a single-particle tight binding calculation, tends to break the bipartite nature of the BLG lattice. We further note that our data exhibits complete symmetry breaking of both spin and pseudospin degeneracy, with fractal gaps appearing for both even and odd values of s and t, whereas only multiples of 4 may be expected in a fully degenerate case. The pseudospin degeneracy, which is related to the spacial inversion symmetry, is lifted due to asymmetric coupling to the substrate, where the bottom graphene layer interacts more strongly with the BN substrate than the top graphene layer. In the high magnetic field regime, Zeeman coupling may break spin symmetry to yield odd integer QHE states. A detailed consideration of these effects can be found in the following section. However, we note that at these fields the Coulomb energy is more than an order of magnitude larger than Zeeman[3], suggesting that interaction-induced spontaneous symmetry breaking of the spin and pseudo-spin degrees of freedom may be necessary to understand our experimental observations.

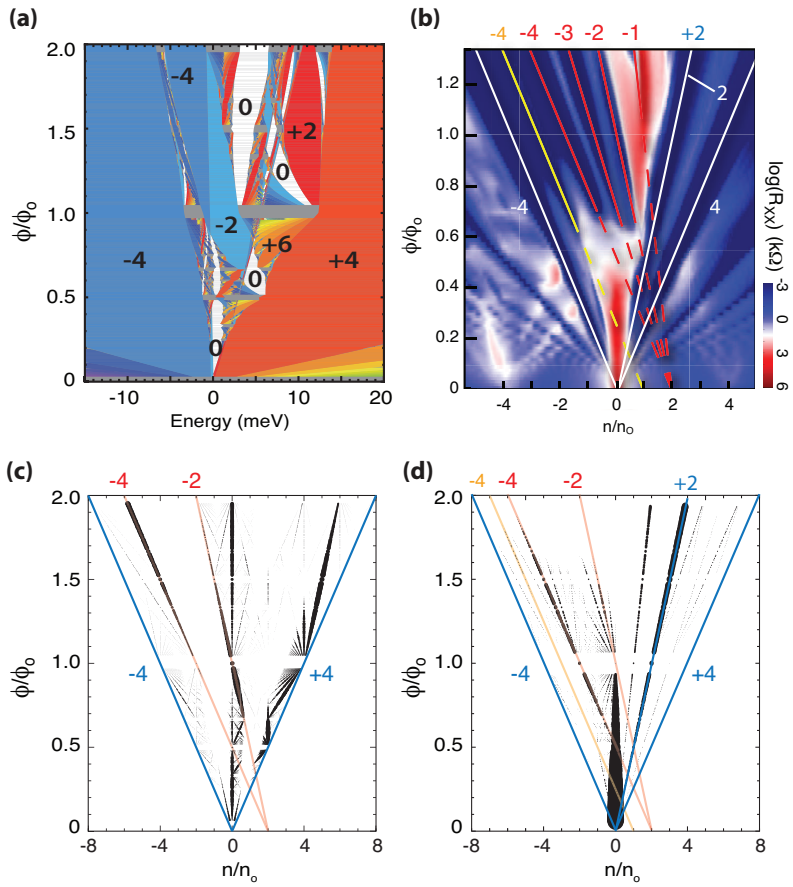

FIG. S4: (a) Energy spectrum calculated for bernal-stacked bilayer graphene on hBN with a 0° mismatch angle. The energy scale is chosen to highlight the lowest Landau level. The numbers label the quantized Hall conductivity in units e^2/h corresponding to each gap. (b) Experimental magnetoresistance measured for device with similar angular mismatch (data is the same as shown in Fig. 2 in the main text). Yellow and red lines correspond to $s = 1$ and $s = 2$, respectively. Numbers along top axis label corresponding t values. (c) Wannier diagram calculated for the energy spectrum in (a), showing only gaps within the lowest Landau level. Horizontal and vertical axes are density and magnetic flux, respectively, normalized to the area of the moiré unit cell. Fractal gaps are plotted as closed black circles where the radius is proportional to the gap width. Coloured lines highlight gaps that are observed in the experimental data. (d) Similar calculation to (b) but including Zeeman coupling and interlayer asymmetry (see text)

S5. THEORETICAL SPECTRUM FOR BILAYER GRAPHENE ON HBN

The Diophantine equation represents a universal set of constraints describing all possible gaps within the Hofstadter spectrum. Which gaps remain open for a particular device depends critically on the details of the system. Fig. S4a shows the calculated Hofstadter spectrum for Bernal-stacked bilayer graphene oriented to hBN. Here graphene and hBN are modeled by tight-binding honeycomb lattices with the lattice periods $a \approx 0.246$ nm and $a_{\mathrm{hBN}} \approx 0.2504$ nm,[5] respectively. We assume that Bernal graphene bilayer and hBN monolayer are aligned with zero rotation angle, and the ratio between the two lattice constants is round to a rational number $a_{\mathrm{hBN}}/a = 56/55$ to give a finite moire superlattice period $56a \approx 13.8$ nm. We assume the interlayer distance of bilayer graphene to be 0.335 nm and that between hBN and graphene 0.322 nm[6]. We consider only a p orbital state on each atomic site, and set on-site potential to 0, 3.34 eV and -1.40 eV for C, B and N atoms, respectively.[7] For the hopping amplitudes between different sites, we adopt the Slater-Koster parametrization used for twisted bilayer graphene[4], irrespective of combination of atoms. To compute the low-energy spectrum in magnetic field, we take the low-lying Landau levels ($|E| < 1.5$ eV) of isolated bilayer graphene as the basis,[4] and the coupling with hBN states in the high-energy region is included as on-site potential on the bottom graphene layer (faced to hBN) in the second-order perturbation.

In Fig. S4b, the energy spectrum is replotted as a Wannier type diagram where the energy axis is replaced by the normalized density. Fractal gaps inside the lowest Landau levels (between $\nu = \pm 4$) are plotted as closed black circles with radius proportional to the gap size. The theoretical calculation correctly predicts the experimentally observed asymmetry in the lowest Landau level (see also Fig. 3 in the main text) where fractal gaps originating from $s > 0$ are much stronger than $s < 0$. Related, the calculation correctly identifies a partial lifting of the 4-fold degeneracy in graphene, evident as features associated with $s = \pm 2$, rather than only multiples of $s = 4$. This results from broken valley degeneracy due to inversion-asymmetric coupling where the bottom graphene layer interacts more strongly with the BN substrate than the top graphene layer. Several details in the theoretical spectrum disagree with experimental observations. For example, strong mini-gaps, predicted on the electron side, are not apparent in the experiment. Additionally, in experiment all symmetries are broken at high field, with fractal gaps corresponding to both odd and even integer values

of s and t appearing, whereas the theoretical spectrum remains two-fold degenerate at all fields since the spin Zeeman splitting is neglected.

In Fig. S4c, the Wannier diagram is recalculated including spin Zeeman splitting ($g = 2$) and interlayer potential difference between the top and the bottom layer of bilayer graphene. The latter is assumed to be the sum of the constant term 30 meV and the gate-induced term proportional to electron density with the relative dielectric constant $\varepsilon_r = 6$. To get a better agreement, we also magnified the coupling strength between graphene and hBN by a factor about 1.4 compared to the original (Fig. S4c). While additional symmetry breaking states appear, exact correspondence with our data is difficult to achieve. The model depends sensitively on physical parameters, such as interlayer coupling strength and interlayer potential difference, that are not well known. Moreover, this model does not account for many-body interaction, which may play a substantial role at these large magnetic fields. Further theoretical and experimental work is necessary to better understand the details of the observed fractal energy spectrum.

S6. STRONG VERSUS WEAK COUPLING

Hofstadter showed[1] that for commensurate fields, corresponding to rational values of $\phi/\phi_0 = p/q$, where p and q are co-prime integers, the single-particle Bloch band splits into q subbands. This approach is referred to as the "strong coupling" limit, where the effect of the periodic electrostatic potential is taken to be large so that the Bloch band description is robust and the effect of the magnetic field is then treated as a perturbation. In the opposite, "weak coupling" limit, one begins with a Landau level and treats the effect of the periodic potential as a weak perturbation. In the second approach, the energy diagram is parameterized by $\phi_o/\phi = q/p$ such that at these same rational values each Landau level splits into p subbands. For the system considered here, we are likely to be in the weak coupling limit since the energy scale of the periodic potential ($\sim$100 K from Fig. 1 in the main text) is much smaller than the energy scale associated with the magnetic fields of interest (*e.g* the cyclotron gap of the lowest LL is $\sim$ 2300 K at 30 T). Importantly, our transport experiment does not access directly the *energy* vs. ϕ/ϕ_o space but rather the *density* vs. ϕ/ϕ_o space. This is an important distinction since, as first demonstrated by Wannier[2], the Diophantine equation, which describes the mini-gaps in the density vs ϕ/ϕ_o space, represents a universal set of constraints that holds true for all system, regardless of superlattice symmetry or weak versus strong coupling. Plotting our experimental data as a Wannier diagram therefore does not explicitly favour one interpretation or the other. Moreover the agreement we find in our experimental data with the Diophantine equation provides support for the more generalized behaviour of electrons subject to both magnetic and spatially varying periodic electric fields predicted by Wannier's interpretation of Hofstadter's original calculation, beyond the specific graphene system considered here. In the main text we choose to plot our data as normalized density vs. ϕ/ϕ_o, however, owing to the universality of the Diophantine equation, we could equivalently plot the data versus ϕ_o/ϕ without any loss of generality and without changing the interpretation of the topological constants, s and t, that appear in the Diophantine equation. Beginning with the Diophantine equation as we wrote it in the main text,

$$(n/n_o) = t(\phi/\phi_o) + s \tag{7}$$

We can simply invert this equation to give

$$(n/n_o)(\phi_o/\phi) = t + s(\phi_o/\phi) \tag{8}$$

which, using the usual definition of Landau level filling fraction, $\nu = n\phi_o/B$ and $n_o = 1/A$, gives

$$\nu = t + s(\phi_o/\phi) \tag{9}$$

Rewritten in this way the role of s and t in the Diophantine equation invert with s becoming the slope and t the intercept of the Wannier diagram. Fig. S5 shows the data from Fig. 3a of the main text plotted against both ϕ/ϕ_o and ϕ_o/ϕ to illustrate this correspondence.

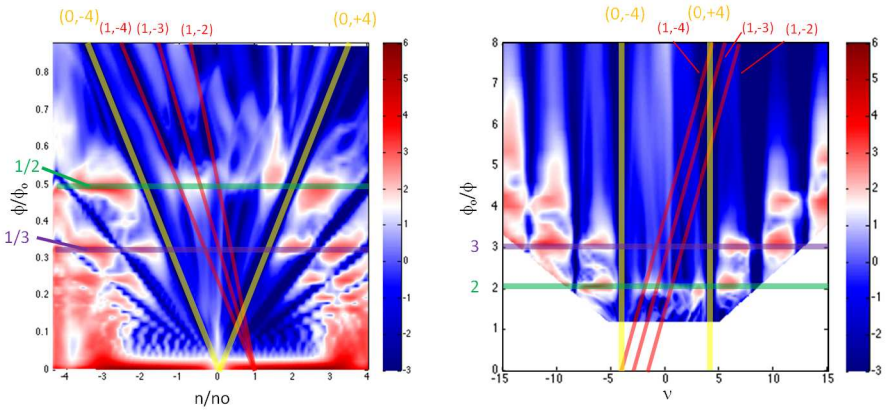

FIG. S5: Left shows data from Fig. 3a of the main text. Right shows this same data replotted against ϕ_o/ϕ. Colored lines represent the same features in both figures, indicating the correspondence when plotting against either axis

S7. TEMPERATURE DEPENDENCE

Gap energies were estimated from the temperature dependence of longitudinal conductivity minima in the thermally activated regime, $\sigma_{xx} \propto e^{\Delta/2k_BT}$ where Δ is the energy gap, k_B is Boltzmann's constant and T is the electron temperature. Each gap value was determined from the corresponding Arrhenius plot by fitting to the linear regime (Fig. S6).

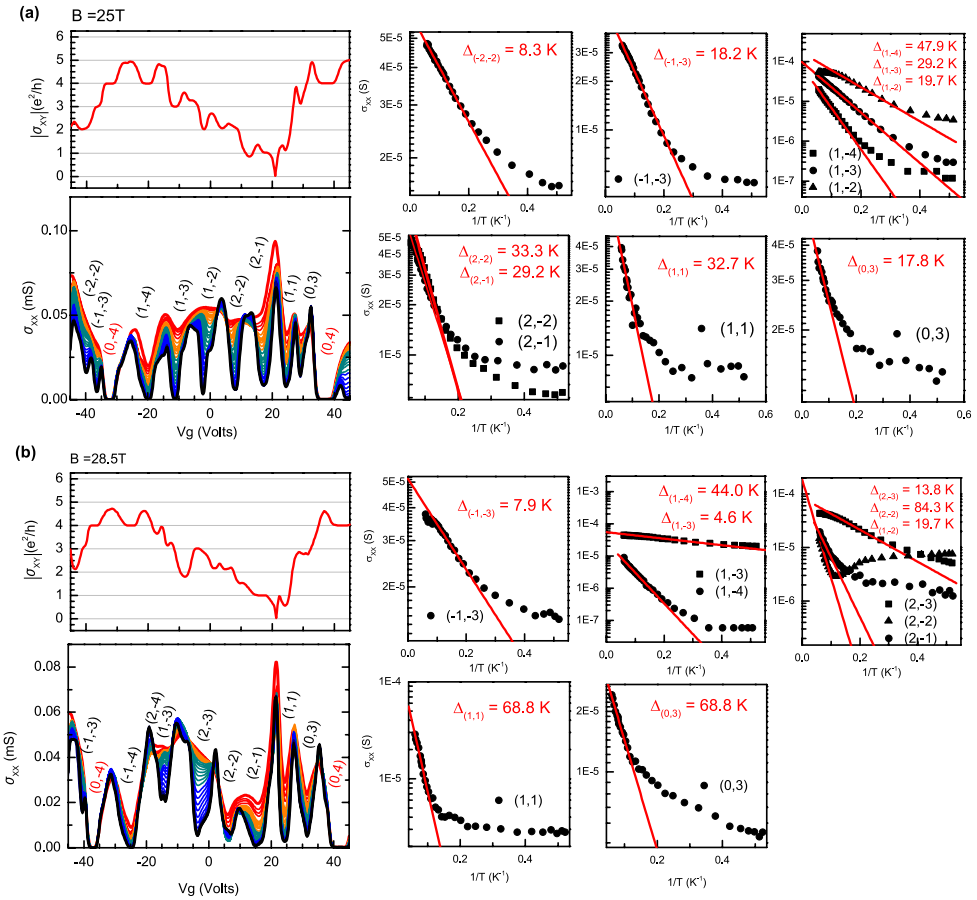

FIG. S6: Temperature dependent transport acquired at (a) $B = 25$ T and (b) $B = 28.5$ T for the device shown in Fig. 3 of the main text. In both (a) and (b) left panel shows the longitudinal conductivity with temperature varying between 2 K and 20 K, together with Hall conductivity at 2 K. Right panel shows Arrhenius plots for each of the fractal gaps labeled in the left panel. The corresponding gap value, determined from the slope in the linear regime, is given in each plot.

[1] Hofstadter, D. *Phys. Rev. B* **14**, 2239–2249 (1976).

[2] Wannier, G. H. *phys. stat. sol. (b)* **88**, 757–765 (1978).

[3] Dean, C. R. *et al. Nature Physics* **7**, 693–696 (2011).

[4] Moon, P. and Koshino, M., Phys. Rev. B **85**, 195458 (2012).

[5] Liu, L., Feng, Y. P. and Shen, Z. X., Phys. Rev. B **68**, 104102 (2003).

[6] Giovannetti, G., *et al.*, Phys. Rev. B **76**, 073103 (2007).

[7] Sławińska, J.,Zasada, I., and Klusek, Z., Phys. Rev. B **81**, 155433 (2010).